

DRAFT VERSION DECEMBER 22, 2022
Typeset using L^AT_EX **manuscript** style in AASTeX62

Hunting for Neighboring Open Clusters with *Gaia* DR3:
101 New Open Clusters within 500 pc

SONGMEI, QIN (秦松梅),^{1,2} JING, ZHONG (钟靖),¹ TONG, TANG (唐通),^{1,2} AND LI, CHEN (陈力)^{1,2}

¹*Key Laboratory for Research in Galaxies and Cosmology, Shanghai Astronomical Observatory, Chinese Academy of Sciences, 80 Nandan Road, Shanghai 200030, China*

²*School of Astronomy and Space Science, University of Chinese Academy of Sciences, No. 19A, Yuquan Road, Beijing 100049, China*

(Received –; Revised –; Accepted –)

Submitted to ApJS

ABSTRACT

We systematically searched for open clusters in the solar neighborhood within 500 pc using pyUPMASK and HDBSCAN clustering algorithms based on *Gaia* DR3. Taking into consideration that the physical size for most open clusters is less than 50 pc, we adopted a slicing approach for different distance shells and identified 324 neighboring open clusters, including 223 reported open clusters and 101 newly discovered open clusters (named as OCSN, Open Cluster of Solar Neighborhood). Our discovery has increased the number of open clusters in the solar neighborhood by about 45%. In this work, larger spatial extents and more member stars were attained for our cluster sample. We provided the member stars and the membership probabilities through

Corresponding author: Songmei Qin, Li Chen
qinsongmei@shao.ac.cn, chenli@shao.ac.cn

the pyUPMASK algorithm for each cluster and derived their astrophysical, age, and structural parameters.

Keywords: Galaxy: open clusters and associations — stars: kinematics and dynamics
— methods: data analysis

1. INTRODUCTION

Open clusters (OCs) in the Milky Way are a collection of stars that are formed from the same molecular cloud and gravitationally bound together (Lada & Lada 2003; Portegies Zwart et al. 2010), thus sharing similar specific characteristics (e.g. age, distance, reddening, and metal abundance, etc.). OCs provide an ideal laboratory for studying star formation and evolution (Evans et al. 2009). Meanwhile, with its large sample, OCs are powerful tracers of the Galactic disk to constrain the Galactic structure and evolution history (Janes & Adler 1982; Dias & Lépine 2005).

As most Galactic OCs are located on the thin disc (Kharchenko et al. 2013), observations for OCs are often hampered by the contamination from dominant background/foreground field stars, leading to more uncertainties in the characterization of cluster properties. Before the Gaia era, reliable member star selection was fairly difficult due to the limited astrometric precision, which brought about inconsistency in the determination of basic parameters like distance, kinematics, and age of OCs (Netopil et al. 2015).

As one of the most successful and ambitious projects, *Gaia* enabled a deluge of scientific work including improving the quality of the cluster census. The *Gaia* DR2 catalog (Gaia Collaboration et al. 2018) presents more than 1.3 billion stars with unprecedented high-precision astrometric and photometric data, greatly improving the reliability of stellar membership determination and characterization of a large sample of OCs. The study of Galactic OCs has ushered in a new era. A more solid assessment of the cluster membership using the precise *Gaia* data greatly promoted subsequent discoveries of new OCs. In the meantime, with the popularity of machine learning, cluster census efficiency has been tremendously raised. Many different methods have been used to search for new or re-detect existing OCs with *Gaia* data, especially various clustering algorithms such as unsuper-

vised photometric membership assignment in stellar clusters (UPMASK, Krone-Martins & Moitinho (2014)), Density-Based Spatial Clustering of Applications with Noise (DBSCAN, Ester et al. (1996)), Hierarchical Density-Based Spatial Clustering of Applications with Noise (HDBSCAN, Campello et al. (2013); McInnes et al. (2017a)), Gaussian Mixture Models (GMMs, Pearson (1894)), Friends of Friends Algorithm (FOF, Huchra & Geller (1982)), etc. Hunt & Reffert (2021) have made detailed comparisons for three main algorithms (DBSCAN, HDBSCAN, GMMs) side-by-side, exploring their effectiveness in blind-searching of OCs with large-scale *Gaia* dataset.

Based on *Gaia* DR2, Cantat-Gaudin et al. (2018) applied the UPMASK algorithm to select cluster members and provided an updated catalog of 1229 OCs including previously reported clusters and 60 newly discovered clusters. Liu & Pang (2019) reported 76 new OCs by employing a FOF-based cluster finder method to hunt out overdensities in the $(l, b, \varpi, \mu_{\alpha}^*{}^1, \mu_{\delta})$ space. In parallel, using the DBSCAN algorithm, Castro-Ginard et al. (2020) found 582 new cluster candidates located in the low galactic latitude area by investigating the aggregation of stars in the 5-dimensional parameter phase space, with part of the candidates overlapped with the result of Liu & Pang. Later on, Cantat-Gaudin et al. (2020) compiled a comprehensive list of 1867 bona fide OCs reanalyzed with UPMASK and *Gaia* data, providing a large and homogeneous catalog of open cluster properties and the corresponding member stars.

As the early stage of *Gaia* third data release, *Gaia* EDR3 (Gaia Collaboration et al. 2021) provides astrometric and photometric parameters of 1.5 billion sources with even higher accuracy than *Gaia* DR2, averagely increasing the precision of proper motion by 2-3 times and parallax by about 20%. Solely based on the *Gaia* EDR3 database, Castro-Ginard et al. (2022) have proposed an OCfinder method, which employs a DBSCAN clustering algorithm for selecting over-densities in the five-dimensional astrometric space and incorporates a deep artificial neural network for distinguishing bona fide OCs in the color-magnitude diagrams (CMDs). In their work, 628 new OCs were picked out, mostly located 1 kpc further away from the Sun. In our recent work (He et al. 2022b), we

¹ $\mu_{\alpha}^* = \mu_{\alpha} \cos \delta$

carried out a blind search for new OCs using *Gaia* DR2/EDR3 by dividing low galactic latitude regions into $2^\circ \times 2^\circ$ ($|b| < 5^\circ$) or $3^\circ \times 3^\circ$ ($|b| > 5^\circ$) grids, sequentially performing the DBSCAN and pyUPMASK clustering algorithms in five-dimensional phase space (d_{l^*} , d_b , v_{α^*} , v_δ , ϖ). Eventually, 541 star clusters unrecorded in literature were found, with a majority of them located beyond 1 kpc from the Sun, while only about 6% are located within 500 pc to the Sun. Using a similar approach and with *Gaia* EDR3, He et al. (2022a) expanded their search grid to $12^\circ \times 12^\circ$ or $18^\circ \times 18^\circ$ to increase the number of clusters in the solar vicinity and cataloged 270 newly found cluster candidates within 1.2 kpc of the Sun, of which 179 new OC candidates are within 500 pc.

In most cases of the above systematic searches for new OCs, *Gaia*'s high-precision position (l , b), proper motion (μ_α^* , μ_δ) and parallax (ϖ) data were used to detect the aggregation characteristics of cluster members in multi-dimensional phase space, photometric data were assisted in confirming the reality of the OCs in the CMD and determining their basic properties by subsequent further analysis. On the other hand, these works have different features on their own methodology and procedure. The newly found objects greatly enrich our understanding of the Galactic OCs population, and they also indicate that the present OCs sample is far from complete. It is anticipated that many new OCs still can be detected through careful analysis of observational data.

The main difficulty in detecting OCs lies in the serious contamination of field stars, especially for nearby OCs, in which member stars cover a wide projected field of view and the proportion of background field stars could be overwhelming. This study aims to find new OCs in the solar neighborhood, with an effective way to decontaminate the background/foreground objects by astrometric data. For this purpose, we proposed a new approach of data ‘‘slicing’’ along the line-of-sight distance. In a systematic search of nearby OCs, we divided all-sky data into sub-blocks with different sizes in every 100 pc interval for reducing contamination of field stars as much as possible and highlighting the aggregation signal of cluster members in the multi-dimensional phase space.

This paper is the first of our serial work, focused on a comprehensive search for undetected clusters within 500 pc from the Sun, solely based on the most recent precise *Gaia* DR3. With our novel ‘‘Slicing’’ approach, we greatly improved the efficiency of detecting the nearby new OCs. Altogether

we updated/derived the physical properties of 324 OCs, with 223 previously reported clusters and 101 newly detected clusters. The data we used in this work is introduced in Section 2. In Section 3, we describe the searching process with the new approach of data “slicing” along the line-of-sight distance. In Section 4, we describe the catalogs of OCs and their members. The discussion about cluster cross-match and property analysis is given in Section 5. Finally, we make a summary in Section 6.

2. DATA

This study aims to find new OCs in the solar neighborhood, with an efficient way of decontaminating the background influences. For this purpose, we restricted our survey to the stars within 500 pc, making full use of the high precision of *Gaia* DR3 data.

Gaia Data Release 3 (*Gaia* DR3; [Gaia Collaboration et al. \(2022\)](#)) provides astrometric information with nearly the same high-precision as *Gaia* EDR3 for about 1.8 billion sources over the sky, as well as near-millimagnitude precision photometric data in three bands (G , G_{BP} and G_{RP}). Moreover, *Gaia* DR3 introduces an impressive wealth of new data products, including the accurate radial velocity parameters for more than 33 million objects ([Katz et al. 2022](#)) and atmospheric parameters (T_{eff} , $\log g$ and $[M/H]$) for about 470 million sources ([Fouesneau et al. 2022](#)). For *Gaia* DR3, the typical proper motion uncertainty respectively goes from 0.07 mas yr^{-1} for $G \approx 17 \text{ mag}$, up to 0.5 mas yr^{-1} for $G = 20 \text{ mag}$, the parallax uncertainty goes from 0.07 mas at $G \approx 17 \text{ mag}$, up to 0.5 mas at $G = 20 \text{ mag}$, and the mean G-band photometry uncertainty goes from 1 mmag at $G \approx 17 \text{ mag}$, up to 6 mmag at $G = 20 \text{ mag}$. It is noteworthy that the newly determined median radial velocities ([Katz et al. 2022](#)) have risen greatly in number compared to *Gaia* DR2 and its median precision goes from 1.3 km s^{-1} at $G_{\text{RVS}} \approx 12 \text{ mag}$, up to 6.4 km s^{-1} at $G_{\text{RVS}} = 14 \text{ mag}$, which greatly help us to study the dynamical evolution of the OCs in the Milky Way.

In this work, we first select stars from *Gaia* DR3 in the region with $|b| < 30^\circ$ since the majority of identified OCs are located in $|b| < 20^\circ$ ([Dias et al. 2002](#); [Kharchenko et al. 2013](#); [Castro-Ginard](#)

et al. 2020). Then, we used the **astroquery.gaia** python package² (Ginsburg et al. 2019) to obtain the positions (l , b), proper motions (μ_α^* , μ_δ), parallaxes (ϖ), magnitudes in three photometric filters (G , G_{BP} and G_{RP}), radial velocity (rv), and their associated uncertainties from *Gaia* Archive³. To investigate the OCs in the solar vicinity, we only retained stars with parallax greater than 2, approximately corresponding to a distance of 500 pc. To reduce the faint background stars, we filtered out stars with $G > 18$ mag. And we applied the cut on re-normalized unit weight error (RUWE) < 1.4 (Lindgren 2018) to exclude the unreliable astrometric and photometric data. Finally, we screened out about 8 million stars as the initial sample.

3. METHOD

Our search process is divided into four steps:

- (1) Partitioning the entire sample into multi-blocks to reduce the contamination of field stars, see details in Section 3.1.
- (2) Employing an unsupervised clustering method pyUPMASK in 5-dimensional data (l , b , ϖ , μ_α^* , μ_δ) to assign probabilities for the stars and remove the stars with probabilities < 0.1 in each block. Then we pick out those blocks that may contain OCs from proper motion distribution features, see details in Section 3.2.
- (3) Separating the stars in each block into members of individual cluster candidates with HDBSCAN, see details in Section 3.3.
- (4) By applying visual inspection on the distribution of position (l , b), proper motion (μ_α^* , μ_δ), magnitude-parallax (G , ϖ), and color-magnitude diagram ($G_{BP} - G_{RP}$, G) of each cluster candidate, we confirm the true existence of the star clusters, see details in Section 3.4.

According to the parameter ranges obtained in the above identification process, we retrieved the astrometric and photometric data for stars in the cluster regions. Then, we obtained the membership

² <https://astroquery.readthedocs.io/en/latest/gaia/gaia.html>

³ <https://gea.esac.esa.int/archive/>

probabilities of stars in each cluster through the pyUPMASK algorithm and regarded the stars with probabilities greater than 0.5 as cluster members, which are cataloged in Table 3.

3.1. Data slicing

Members of an open cluster that formed in the same molecular clouds, generally are severely immersed in a dense star field and it is hard to distinguish the actual star cluster members from the background, especially for those clusters mixed with the vast majority of field stars. The most efficient way of hunting out new clusters is to look for the clustering of stars in the velocity space (i.e. the vector-point-diagram) since open cluster members share a distinctive movement as compared to the field stars. For highlighting the cluster members in the proper motion distribution diagram, we cut the entire sample into various sub-samples according to their 3D spatial coordinates (l , b , and ϖ). For example, as we can see in Figure 1, the two panels are the proper motion distributions (μ_α^* , μ_δ) of two sub-samples with the same 2D spatial distribution range: $306^\circ \leq l \leq 312^\circ$ and $-6^\circ \leq b \leq 0^\circ$. The ϖ of the left sample is greater than 1.5, in the red dashed circle we can see a vaguely condensed area blurred by the overwhelming distribution of field stars. In the right panel of Figure 1, we limited this sample to $2 < \varpi < 2.5$, thus removing many foregrounds and background stars and the corresponding distribution shows an obvious concentration of cluster member stars around the same region. Hence, ingenious data slicing is critical for hunting out new OCs in our cluster searching volume.

To more fully and efficiently reveal OCs hidden in the field stars, we divided the entire remaining stellar sample within the Galactic latitude range of $|b| < 30^\circ$ into 1044 blocks according to their 3D spatial coordinates (l , b , and ϖ). Firstly, We separated all the stars into several searching shell regions along the ϖ (> 10 mas, 5-10 mas, 3.33-5 mas, 2.5-3.33 mas, 2-2.5 mas), approximately corresponding to the distance (< 100 pc, 100-200 pc, 200-300 pc, 300-400 pc, 400-500 pc), which is large enough to cover at least one typical open cluster. In recent years, many investigations based on *Gaia* data revealed that besides the high-density inner parts, there might be extended low-density outer halos (Zhong et al. 2019; Meingast et al. 2021; Zhong et al. 2022) or elongated tidal tails (Carrera et al. 2019; Zhang et al. 2020; Bai et al. 2022; Boffin et al. 2022) in the outskirts of the OCs. To adequately

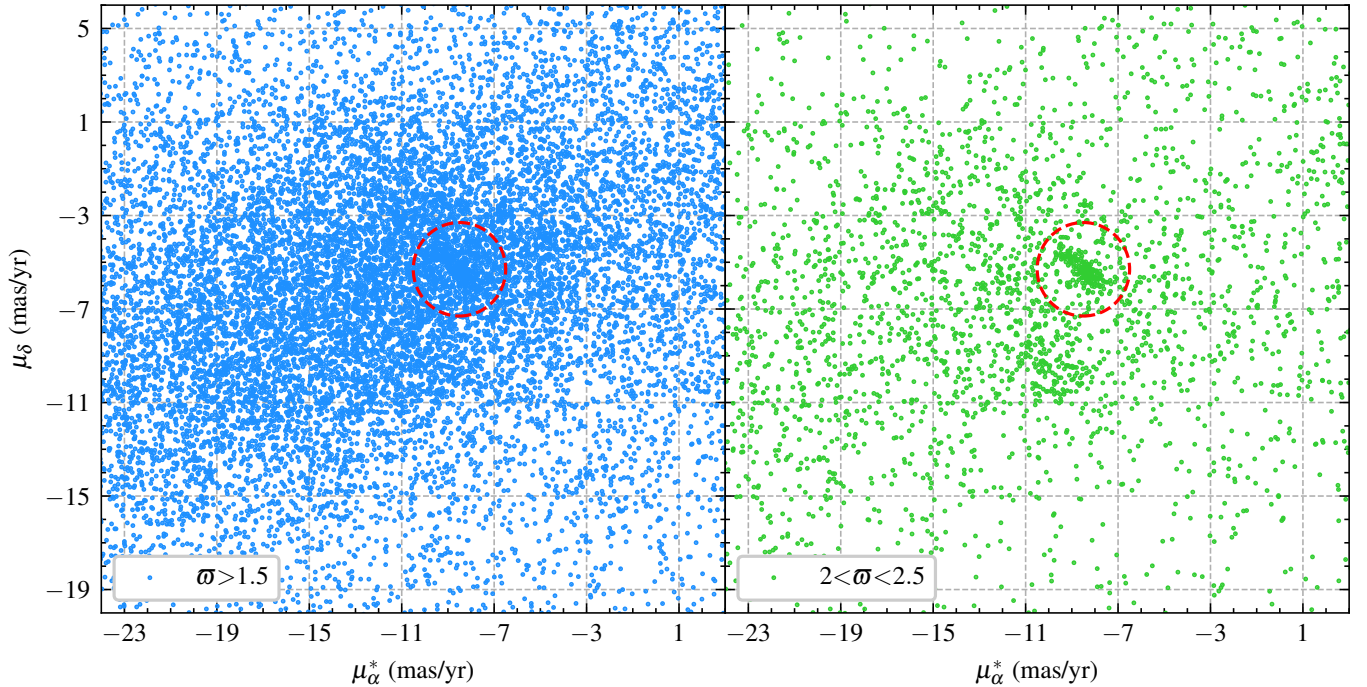


Figure 1. The proper motion distribution of two samples. The blue and green dots refer to stars with different distant slicing. The red dashed circles represent the OC where the members assembled.

contain the outer halo structure of OCs, we adopted 50 pc as the typical extended spatial scale of OCs (Tarricq et al. 2022; Zhong et al. 2022). As the projected angular size varies with distance, we adopted the searching grids with different angular sizes, ranging from 30° at a close distance of 100 pc to about 6° at 500 pc, as listed in Table 1.

Table 1. Size of the search area.

dist (pc)	<100	100-200	200-300	300-400	400-500
ϖ (mas)	>10	5-10	3.33-5	2.5-3.33	2-2.5
size (deg)	30	20	12	10	6

3.2. Initial screening with *pyUPMASK*

After getting the 1044 slicing blocks, we applied the *pyUPMASK* algorithm (Pera et al. 2021) to gain membership probabilities of each star, which is based on the clustering of members compared

to field stars in $(l, b, \varpi, \mu_\alpha^*, \mu_\delta)$ phase space. pyUPMASK is an open-source software package compiled by Python language following the development principle of UPMASK (Krone-Martins & Moitinho 2014), which is a member star determination method developed to process photometric data originally, though later widely used in the determination of member stars based on astrometric data (Cantat-Gaudin et al. 2018, 2020).

This enhanced clustering method contains several major procedures as follows: (i) Input data reduction using Principal Component Analysis (PCA); (ii) Choose one of the clustering algorithms such as K-means(Chaturvedi et al. 2001), mini-batch k-means (MBK, Sculley (2010)), Gaussian mixture models (GMM, Pearson (1894)), agglomerative clustering (AGG, Zepeda-Mendoza & Resendis-Antonio (2013)), the nearest neighbors density method (KNN, Rodriguez & Laio (2014)), Voronoi (VOR, Voronoi (1908)) method supported by pyUPMASK to process the reduced data; (iii) Employ Ripley’s K function (Ripley 1976) to assess the authenticity of the clusters (or reject the fake clusters with a random uniform distribution); (iv) Apply the Gaussian-Uniform Mixture model to level down the field contamination. We skip this step to reserve those poor or non-Gaussian distribution clusters; (v) Evaluate the cluster membership probabilities through the kernel density estimator (KDE).

The continuous KDE probabilities between 0 and 1 are assigned to all the stars defined as $P_{cl} = KDE_m / (KDE_m + KDE_{nm})$, where KDE_m and KDE_{nm} refer to the KDE likelihoods for the members and nonmembers, and this reflects the proportion of true cluster stars and field stars. Concerning the imbalance of members and field stars that are mixed within a stellar cluster field, we set the lower limit of member probabilities to 0.1 to preserve cluster members as many as possible. As an example, Figure 2 shows the position and proper motion distributions of a sample with the range of $160^\circ \leq l \leq 180^\circ$, $-30^\circ \leq b \leq -10^\circ$ and $5 \text{ mas} < \varpi < 10 \text{ mas}$. In Figure 2, grey dots represent stars with probabilities less than 0.1 (about 90%), while the rest colored dots represent stars with probabilities greater than 0.1 (about 10%). We can see that after rejecting a large proportion of field stars, some clumps are exposed in the position and proper motion distributions. Nevertheless, some clusters such as the Cand1 in Figure 3 show a relatively sparse spatial distribution that leads

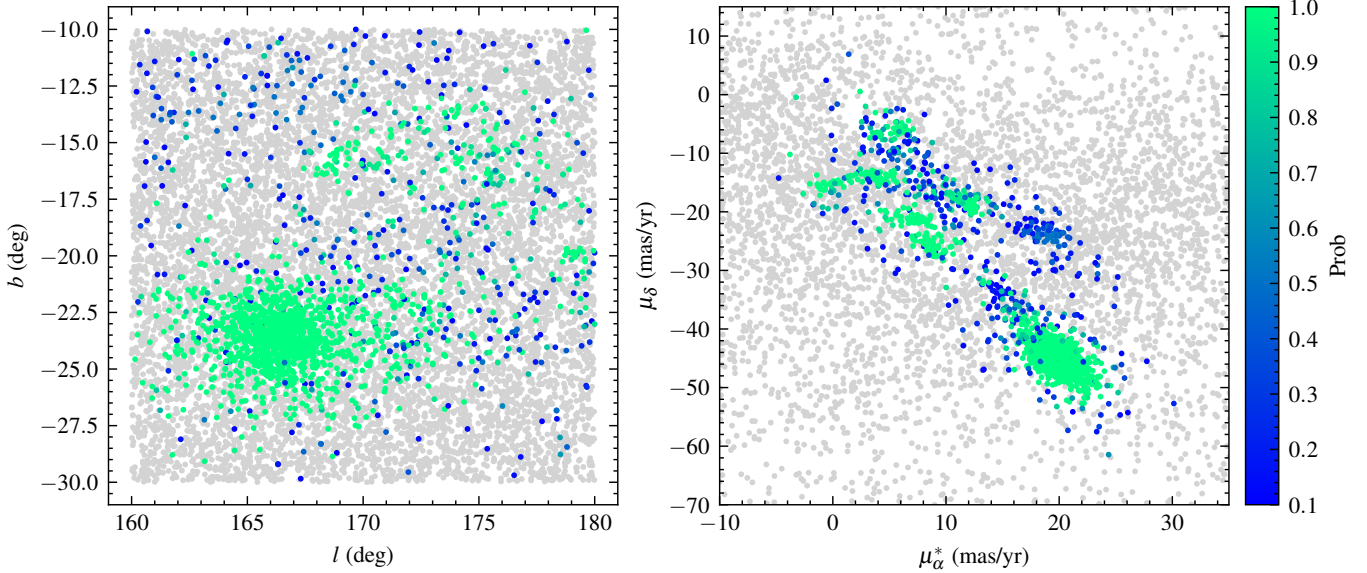


Figure 2. Position and proper motion distributions of one block sample. The grey dots refer to the stars with membership probabilities less than 0.1, while the colored dots are stars with membership probabilities greater than 0.1. The color bar represents the probabilities of member stars.

to lower probabilities. To avoid losing such sparse OCs, we applied the cut at probability > 0.1 to exclude most field stars.

After excluding field stars with low probability ($p < 0.1$) in all block samples, we visually inspected the proper motion distributions of member stars. As shown in Figure 2, the block sample exhibits several distinct clumps both in position and proper motion distribution, which would be reserved in the following analysis in Section 3.3. It is noticed that, the concentrated structure around $(20 \text{ mas yr}^{-1}, -45 \text{ mas yr}^{-1})$ is the famous open cluster Pleiades (M 45) (Cantat-Gaudin et al. 2020; Heyl et al. 2022). Eventually, 394 block samples that might contain OCs were retained.

3.3. Separating OCs with HDBSCAN

For the 394 samples, we normalized the data in 5 dimensions ($l, b, \varpi, \mu_\alpha^*, \mu_\delta$) and then used the HDBSCAN (McInnes et al. 2017b) to separate individual cluster candidate members from field stars. HDBSCAN is primarily proposed by Campello et al., which combines the density-based approach of DBSCAN (Ester et al. 1996) with hierarchical clustering to deal with datasets of varying densities. The key parameter to affect the resulting clustering is *min_cluster_size* (m_{clSize}), which refers to the

minimum possible size of a cluster. The smaller value of m_{clSize} might cause a large cluster to be divided into small clumps, which may generate some fake clusters. However, with a larger value of m_{clSize} , small adjacent clusters in phase space would be combined as a big one.

Hunt & Reffert (2021) compared three clustering algorithms DBSCAN, HDBSCAN and GMMs in computational speed and availability, and concluded that HDBSCAN is the most sensitive and effective method for revealing OCs in *Gaia* data. In their work, the performance of the HDBSCAN algorithm for 100 OCs showed that the value of “Sensitivity” = TP / (TP + FN) was the largest when adopted m_{clSize} as 10, which corresponds to the strongest ability of HDBSCAN to detect real OCs. Campello et al. (2013) also recommended setting $m_{clSize} = m_{Pts} = 10$ for best sensitivity and speed when running the algorithm. Thus, we assigned $m_{clSize} = 10$. At the same time, for better detecting some sparse OCs, we selected the “leaf” cluster selection method (McInnes et al. 2017b). After applying HDBSCAN to separate out cluster groups in 5-dimension data, we obtained 800 OC candidates. For example, in Figure 3, the same sample stars as in Figure 2 were separated into eight cluster candidates with HDBSCAN. Although some fake clusters may arise because of the parameter selection in HDBSCAN, we will check every cluster candidate in 5-dimension data by eyes, see details in Section 3.4.

3.4. Visual inspection

The member stars in an OC are co-moving and sharing similar parallax/distance. In the meantime, the color-magnitude diagram of the members is expected to present a clear main-sequence feature. We visually screen each cluster candidate in terms of position (l , b), proper motion (μ_α^* , μ_δ), magnitude-parallax (G , ϖ) distributions and color-magnitude diagram ($G_{BP} - G_{RP}$, G) to reject the “false positive” clusters.

It is noticed that a given cluster candidate may happen to be identified within one block, sometimes may fall on the borders, or can be detected in more than one block (with different membership results). To merge the split cluster candidates, we adopted the following process. We designated a nearby cluster with the smallest angular distance as a reference cluster for each target cluster identified by eye inspection. And we inspected the position (l , b), proper motion (μ_α^* , μ_δ), magnitude-parallax (G ,

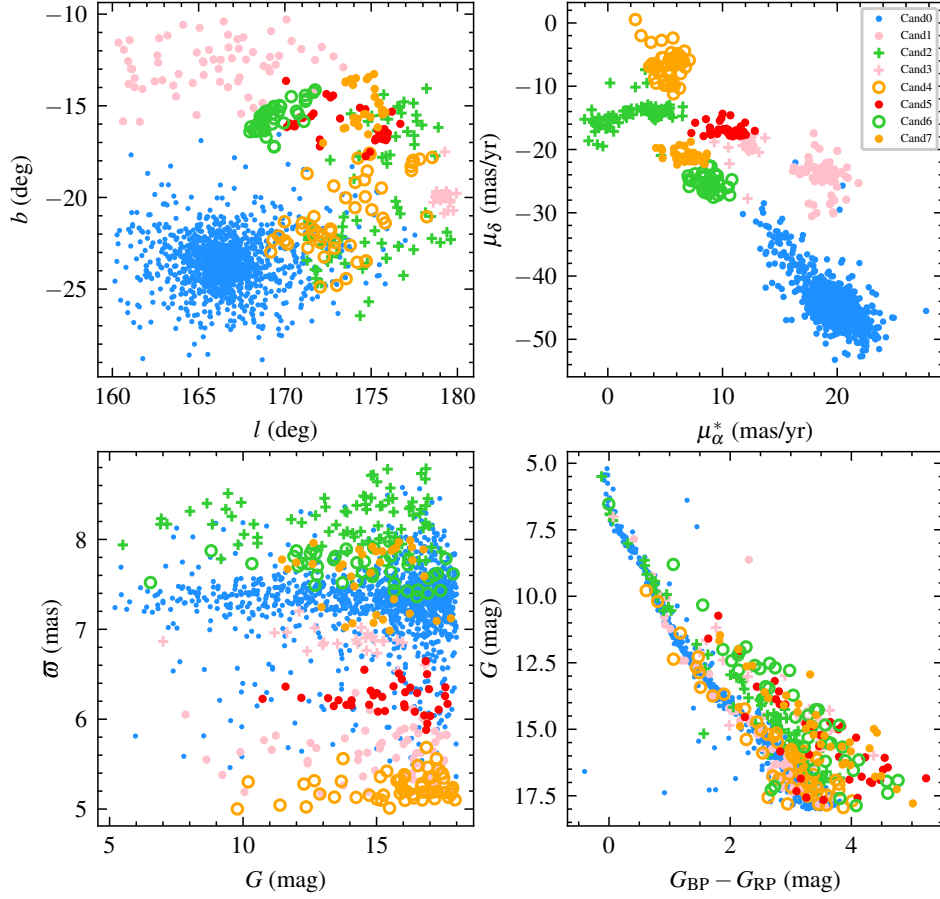


Figure 3. Spatial (l , b), proper motion (μ_α^* , μ_δ), magnitude-parallax (G , ϖ), color-magnitude ($G_{BP} - G_{RP}$, G) diagrams of the eight separated cluster candidates using HDBSCAN. Colors and symbols represent member stars of different cluster candidates.

ϖ) distribution and color-magnitude diagram ($G_{BP} - G_{RP}$, G) of the target and reference clusters together to assess whether they are the same cluster or not. A few specific cases that arose in our cluster samples are listed as follows:

- (a) Only one peak appears in both spatial and proper motion distributions. If the parallaxes of their members are consistent, the two clusters are thought to be combined together; if not, the two clusters are considered to be different individuals.
- (b) More than one peak arises in both spatial and proper motion distributions. In this case, the two clusters are regarded as different individuals.

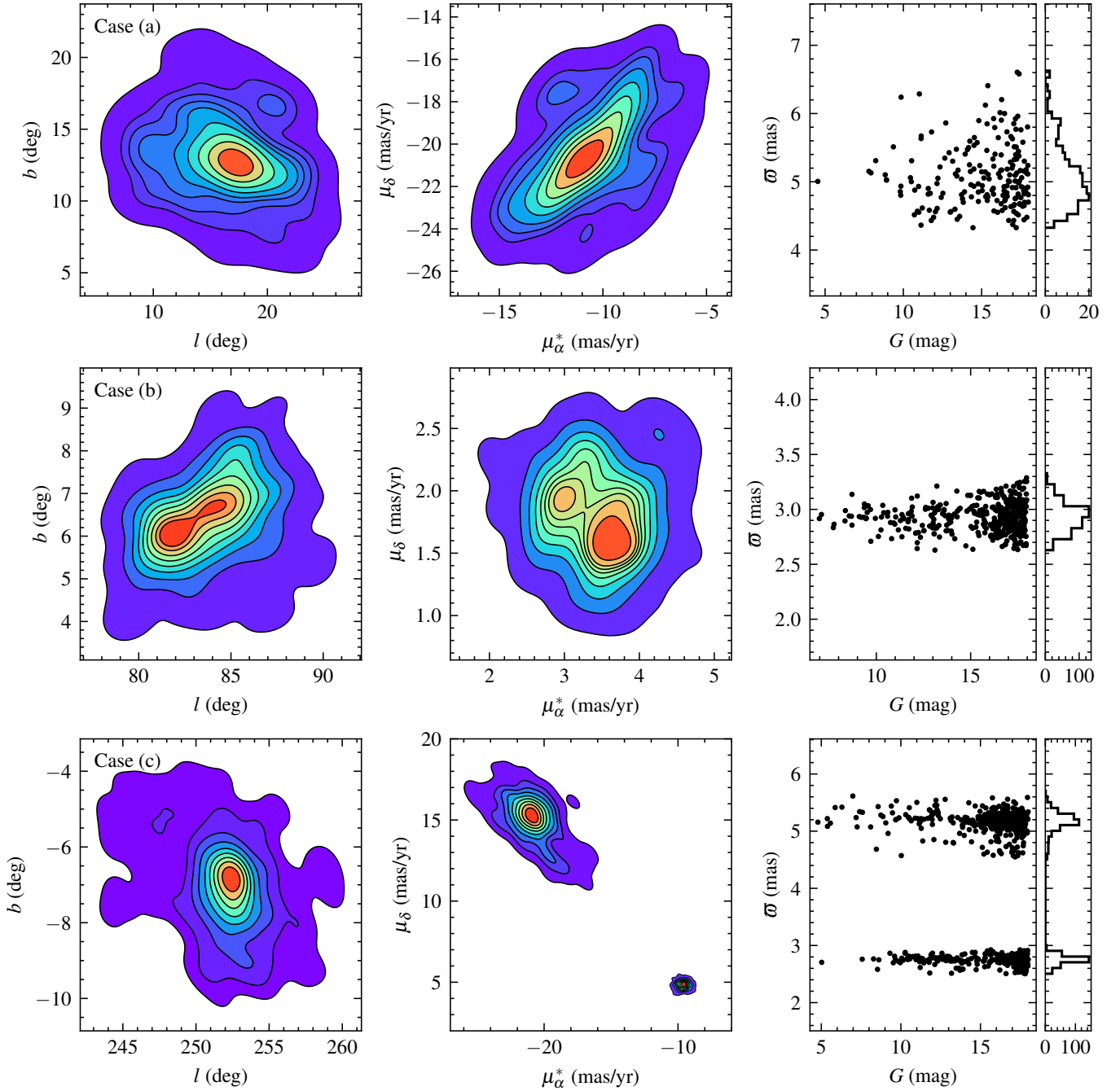


Figure 4. Three examples of target and reference clusters. The left panels present the spatial distributions of members' iso-density contours. The middle panels present the proper motion distribution of members' iso-density contours. The right panels present the G -parallax distribution with parallax histograms on the right edge.

- (c) Only one peak in the spatial distribution but two separated peaks in the parallax histogram. They are identified as distinguished clusters.

Figure 4 shows 5-dimensional distributions of three corresponding examples. The example of the case (a) is presented in the top panel: only one spatial over-density distribution can be detected and one peak in the proper motion distribution. In addition, there is one peak around 5 mas in the parallax histogram. These properties demonstrate that all members belong to the same cluster. The middle panels display the case (b) example of two clusters, which hold close but notably different peaks. And their mean parallaxes are approximately equal to 2.9 mas. They could be binary clusters at nearly the same distance. To illustrate the case (c), we show two distinct clusters which have the same projected position in the bottom panel. Although these clusters overlap in the projected position, which means one is in the front and the other is in the back, they can be well distinguished through the distribution of different proper motions and parallaxes. During the above visual checking process, we adjusted the parameter ranges of each cluster. Finally, we obtained 324 genuine stellar aggregations, most of which are certainly OCs.

4. CLUSTER AND MEMBER CATALOGUE

We regarded stars with membership probabilities > 0.5 as cluster members. Based on those members, we attained the cluster properties. We provided two catalogs⁴ in this paper: one for the properties of 324 OCs and the other for parameters of 59304 member stars.

Table 2 describes the catalog of our open cluster properties. Cross-matching with the published catalogs, we verified the reported and new OCs and provided their OCSN “Names” (Cols. 1). The “OC_flag” (Cols. 2) was given according to the cross-matching cases, see details in Section 5.1. The central coordinates of clusters (Cols. 3-6) were obtained through a two-dimensional Gaussian kernel density estimator (KDE) and the bandwidth of the kernel was calculated via the well-known Scott’s rule (Scott 1992, 2015). We derived the mean values of proper motion and parallax of each cluster and their corresponding standard deviations as well (Cols. 7-12). Meanwhile, we fitted the mean

⁴ The complete catalogs are available on CDS.

radial velocity for each cluster through the Gaussian profile (Cols. 13-16). By visually inspecting the match of the isochrones to the observed cluster CMDs, we further obtained the age, distance modulus, and reddening parameters (Cols. 18-20). In order to better reveal the structural characteristics of nearby star clusters, we provided the radii parameters (r_c, r_t, r_o, r_e) of OCSN clusters (Cols. 22-29) according to the two-component model proposed by [Zhong et al. \(2022, hereafter Zhong2022\)](#). We listed the reported cluster names in the literature as well as the corresponding reference work (Cols. 30-31).

Table 3 describes the catalog of cluster members, including the astrometric and photometric parameters from the *Gaia* DR3 (Cols. 1-20), the derived membership probabilities through pyUPMASK (Cols. 21), and the corresponding cluster names in this work (Cols. 22).

4.1. Radial velocity of OCs

In our cluster member sample, there are a total of 22067 stars with radial velocities from *Gaia* DR3 ([Katz et al. 2022](#)), which can be used to estimate the mean radial velocities (RVs) of 324 clusters. At first, we found that the RVs of the initial cluster members deviate greatly from the median value, especially at $G > 14.5$ mag. It is noticed that a similar situation was also reported by [Ye et al. \(2022\)](#). To derive the reliable mean radial velocity of each cluster, we removed the outliers beyond 3σ and used the high-quality members for calculation. The RV outliers, high-quality members and non-RV members are labeled as “rv_Flag” = 0, 1, 2 respectively in the member catalog (see Table 3). In our sample, the average RVs were derived by the Gaussian fitting for clusters with enough RVs members or simply provided by median RVs for clusters with few RVs members, while the corresponding uncertainties were the 1σ of the Gaussian functions or standard deviations, respectively. We provided the corresponding “RV_Flag” = 1 for mean RVs of Gaussian-fitting and 2 for median RVs. Eventually, there are 324 OCs with observed mean or median radial velocity (hereafter *Gaia* DR3 RVs) which are listed in Table 2.

Table 2. Description of the catalog of open cluster properties.

Column	Format	Unit	Description
Name	string	-	Cluster name in this work
OC_flag	string	-	Cluster cross-match cases
glon	float	deg	Mean galactic longitude of members
glat	float	deg	Mean galactic latitude of members
ra	float	deg	Mean right ascension of members
dec	float	deg	Mean declination of members
pmra	float	mas yr ⁻¹	Mean proper motion in right ascension of members
e_pmra	float	mas yr ⁻¹	Standard deviation of proper motion in right ascension
pmdec	float	mas yr ⁻¹	Mean proper motion in declination of members
e_pmdec	float	mas yr ⁻¹	Standard deviation of proper motion in declination
plx	float	mas	Mean parallax of members
e_plx	float	mas	Standard deviation of parallax
RV	float	km s ⁻¹	Mean radial velocity of members
e_RV	float	km s ⁻¹	Standard deviation of radial velocity
RV_Flag	string	-	Label of RV
N_RV	int	-	Number of RV members
N	int	-	Number of members with membership probabilities higher than 0.5
m-M	float	mag	Cluster distance modulus determined by the isochrone fit
logt	float	-	Cluster age determined by the isochrone fit
E(B-V)	float	mag	Cluster reddening determined by the isochrone fit
r_h	float	deg	Angular size of half number radius
r_c	float	deg	Cluster core radius
e_r_c	float	deg	Uncertainty of cluster core radius
r_t	float	deg	Cluster tidal radius
e_r_t	float	deg	Uncertainty of cluster tidal radius
r_o	float	deg	Mean radius of cluster outer region
e_r_o	float	deg	Uncertainty of the mean radius of cluster outer region
r_e	float	deg	Cluster boundary radius
e_r_e	float	deg	Uncertainty of cluster boundary radius
Ref_Name	string	-	Cluster names in the literature works
Ref	string	-	References corresponding to cluster names (see Section 5.1)

Table 3. Description of the catalog of cluster members.

Column	Format	Unit	Description
Source_id	long	-	Unique source identifier
l	double	deg	Galactic longitude
b	double	deg	Galactic latitude
ra	double	deg	Right ascension (J2016)
dec	double	deg	Declination (J2016)
plx	double	mas	Parallax
plx_err	float	mas	Standard error of parallax
pmra	double	mas yr ⁻¹	Proper motion in right ascension
pmra_err	float	mas yr ⁻¹	Standard error of proper motion in right ascension
pmdec	double	mas yr ⁻¹	Proper motion in declination
pmdec_err	float	mas yr ⁻¹	Standard error of proper motion in declination
rv	float	km s ⁻¹	Radial velocity
rv_err	float	km s ⁻¹	Radial velocity error
rv_Flag	string	-	Label of radial velocity members
Gmag	float	mag	G magnitude
Gmag_err	float	mag	G magnitude error
BPmag	float	mag	BP magnitude
BPmag_err	float	mag	BP magnitude error
RPmag	float	mag	RP magnitude
RPmag_err	float	mag	RP magnitude error
probs	double	-	Membership probability obtained from pyUPMASK
Name	string	-	Corresponding cluster name in this work

At the same time, we calculated the mean or median RVs of our cluster samples with APOGEE DR17 (Abdurro'uf et al. 2022) and LAMOST DR9 of Medium Resolution survey ⁵ (hereafter APOGEE RVs and LAMOST-MRS RVs) through the same approach. The comparisons of the RVs

⁵ <http://www.lamost.org/dr9/>

for 55 common OCs between *Gaia* DR3 and APOGEE, 42 common OCs between *Gaia* DR3 and LAMOST-MRS are shown in Figure 5. The mean and standard deviation values of the differences between *Gaia* DR3 RVs and APOGEE RVs are -1.42 km s^{-1} and 2.83 km s^{-1} , and the corresponding values of the differences between *Gaia* DR3 RVs and LAMOST-MRS RVs are -0.48 km s^{-1} and 1.50 km s^{-1} , demonstrated as the red dashed lines and the grey-filled regions in Figure 5. It is evident that *Gaia* DR3 RVs, APOGEE RVs and LAMOST-MRS RVs are mostly consistent.

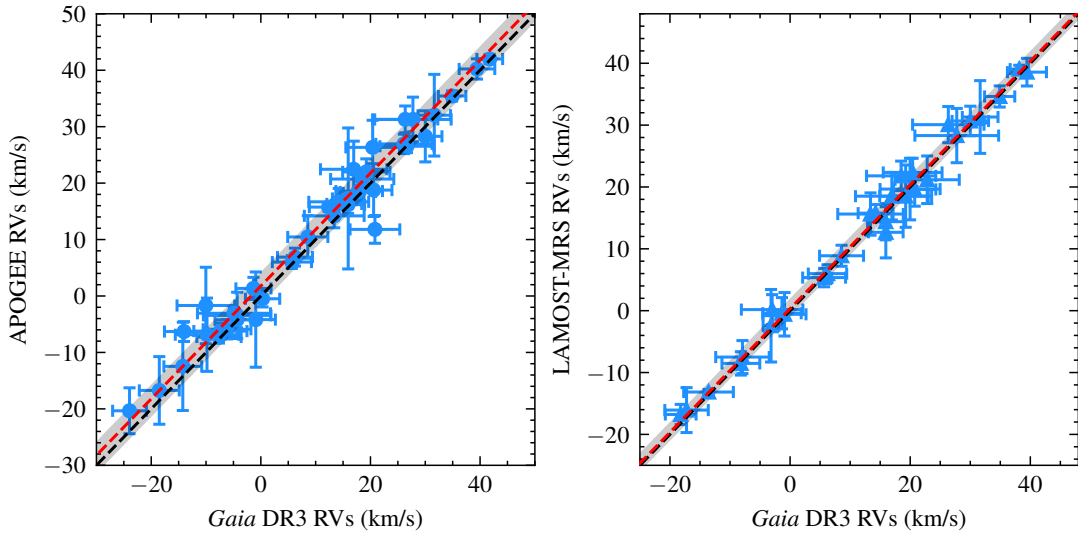


Figure 5. The open cluster mean RVs comparison between *Gaia* DR3 and APOGEE/LAMOST-MRS. The error bars of blue points/triangles are the 1σ of the Gaussian fitting or standard deviations for open cluster RVs. The black dashed lines are 1:1 scale lines. The red dashed lines are the mean values of the differences between *Gaia* DR3 RVs and APOGEE RVs or LAMOST-MRS RVs, and the grey-filled regions are the corresponding 1σ regions.

4.2. Metallicity and Isochrone fitting

Before getting the age parameters for our OC samples, we also collected available $[\text{Fe}/\text{H}]$ metallicity for clusters from literature spectroscopic work. The Open Cluster Chemical Abundances and Mapping (OCCAM) survey (Donor et al. 2020, hereafter Donor2020) provided the $[\text{Fe}/\text{H}]$ abundances for a sample of 128 OCs from the APOGEE DR16. After cross-matching our cluster samples with Donor2020, 14 common clusters were found. We also acquired 7 common clusters within 500 pc from

(Netopil et al. 2022, hereafter Netopil2022). In addition, we gathered the LAMOST spectroscopic parameters of the other 34 OCs from Zhong et al. (2020, hereafter Zhong2020). To ensure the reliability of [Fe/H] for OCs, we select 31 OCs with more than 5 [Fe/H] members, as shown in Table 4, which would be used in the following isochrone fitting process.

To determine the age parameter of the OCs found in the solar neighborhood, we use a set of Padova isochrones (Marigo et al. 2017) to perform the CMD fitting. The grid of logarithm ages in isochrones is from 6.0 to 10.10 with an interval of 0.05, and the photometric system is the *Gaia* photometric system (Riello et al. 2021) from CMD 3.6⁶. For clusters whose metallicity is reported by literature, we adopted the abundances in Table 4 as an input parameter to derive the Padova isochrone, while the isochrones of other clusters were adopted with the solar metallicity $Z_{\odot} = 0.0152$ (Caffau et al. 2009, 2011). We carefully inspected the match of the isochrones to the significant characteristic regions, such as the upper main sequence, the turn-off point, and the red giant or red clump features in the CMDs. By adjusting the isochrones to achieve the best fitting of cluster members in the CMDs, we obtained the age, distance modulus as well as reddening of each cluster. Then, we use the formula $A_G = 2.74 \times E(B - V)$, $E(BP - RP) = 1.339 \times E(B - V)$ and $E(G - RP) = 0.705 \times E(B - V)$ (Casagrande & Vandenberg 2018; Zhong et al. 2019) to calculate the E(B-V) values. Figure 6 shows the isochrone-fitting examples for four clusters⁷ and the final fitting results (age: logt; distance modulus: m-M; reddening value: E(B-V)) are shown in the Table 2.

4.3. Structural parameters

It is evident that the discoverable spatial scale of OCs is greatly expanded in the Gaia era. More and more members located in the extended region were identified through their kinematic properties (Meingast & Alves 2019; Meingast et al. 2021). Our investigation of nearby clusters also shows that many clusters have an extended outer structure. Many reported clusters are just tight core components in our OCSN catalog (See Section 5.1).

⁶ <http://stev.oapd.inaf.it/cgi-bin/cmd>

⁷ The complete isochrone-fitting figure set (324 clusters) is available in the online Journal.

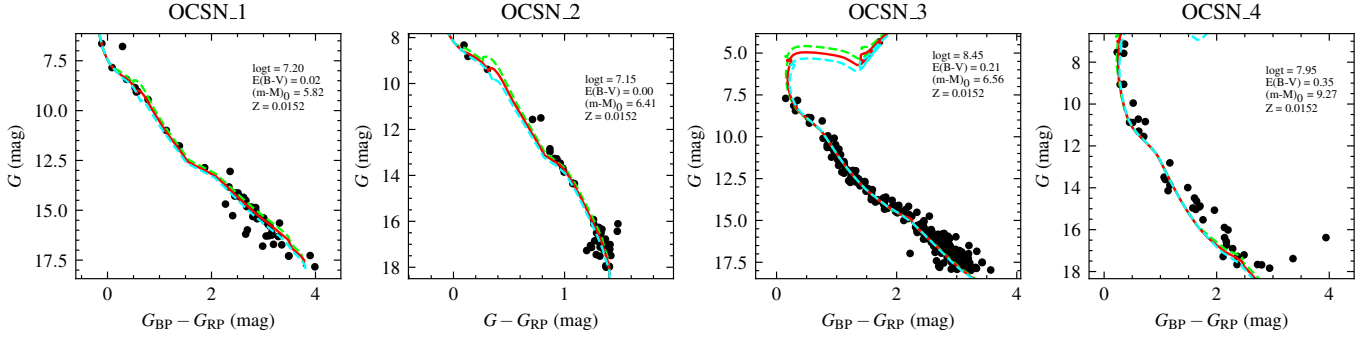


Figure 6. Example of ischrone-fitting results for four clusters: OCSN_1, OCSN_2, OCSN_3, OCSN_4. The black dots refer to the members identified in this work. The red solid lines indicate the best-fitting isochrones while the lime or cyan dashed lines denote the isochrones whose ages (logt) are 0.5 larger or smaller than the best-fitting isochrones. All the isochrones applied the same solar metallicity ($Z_{\odot} = 0.0152$). The best fitting parameters are shown in the panels for each cluster.

To better describe the radial density profile (RDP) of clusters with extended outer regions, it is proposed by Zhong2022 of using a two-component model instead of only using a King model (King 1962, 1966). After deriving the RDP of each cluster through a two-dimensional Gaussian KDE on the spatial space, we further attempted the two-component model to fit the RDP:

$$F(r) = f(r) + g(r) \quad (1)$$

where $f(r)$ is the King model that mainly described the RDP of core members and $g(r)$ is a logarithmic Gaussian function that described the RDP of corona members (Zhong et al. 2022).

In the fitting procedure, the two-component model performs a more reliable approximation of the RDP of most OCSN clusters. In particular, we noted that there are about 33% of OCSN clusters whose RDP can be well approximated by the single King model. The fraction of clusters that well follow a single King profile is larger than the fraction (about 10%) in Zhong2022. We speculate that it is because the outer extended structure of some nearby clusters can be extended to dozens of degrees, the OCSN clusters we identified may still be the core components. However, there are still a fraction of star clusters (43 of 324) that cannot be decently fitted by the single-component or two-component method, possibly due to their sparse distribution or extended tail-like structures or even multiple cores. And it is quite obviously that not all of the OCSN clusters have a clear core.

Table 4. Metallicity of some reported clusters.

Name	Ref_Name	[Fe/H] (dex)	$\sigma_{[Fe/H]}$ (dex)	$N_{[Fe/H]}$	Ref
OCSN_127	ASCC_16	-0.06	0.06	33	Donor2020
OCSN_128	ASCC_19	-0.07	0.05	19	Donor2020
OCSN_129	ASCC_21	-0.13	0.04	10	Donor2020
OCSN_130	ASCC_41	-0.11	0.07	8	Zhong2020
OCSN_141	Alessi_20	+0.14	0.04	11	Zhong2020
OCSN_189	Collinder_69	-0.10	0.05	55	Donor2020
OCSN_192	Collinder_350	-0.10	0.11	31	Zhong2020
OCSN_194	Gulliver_6	-0.13	0.20	18	Zhong2020
OCSN_203	IC_348	-0.17	0.14	11	Zhong2020
OCSN_204	IC_2391	-0.03	0.04	11	Netopil2022
OCSN_205	IC_2602	-0.02	0.02	7	Netopil2022
OCSN_206	IC_4665	-0.01	0.02	11	Netopil2022
OCSN_207	IC_4756	+0.02	0.04	13	Netopil2022
OCSN_213	L_1641S	-0.09	0.07	22	Donor2020
OCSN_218	Melotte_20	+0.01	0.05	64	Donor2020
OCSN_219	Melotte_22	0.00	0.05	83	Donor2020
OCSN_220	Melotte_25	+0.12	0.04	48	Netopil2022
OCSN_221	NGC_752	-0.08	0.07	49	Zhong2020
OCSN_222	NGC_1039	+0.02	0.06	7	Netopil2022
OCSN_224	NGC_1662	-0.19	0.09	35	Zhong2020
OCSN_226	NGC_1980	-0.08	0.04	9	Donor2020
OCSN_227	NGC_2232	-0.09	0.09	6	Zhong2020
OCSN_228	NGC_2281	-0.08	0.11	73	Zhong2020
OCSN_234	NGC_2632	+0.16	0.07	21	Netopil2022
OCSN_241	NGC_6633	-0.10	0.05	8	Zhong2020
OCSN_255	RSG_1	-0.01	0.09	20	Zhong2020
OCSN_256	RSG_5	+0.07	0.09	13	Zhong2020
OCSN_259	Roslund_6	-0.01	0.10	32	Zhong2020
OCSN_261	Ruprecht_147	+0.12	0.03	33	Donor2020
OCSN_265	Stock_2	-0.11	0.07	19	Zhong2020
OCSN_266	Stock_10	-0.13	0.09	23	Zhong2020

5. DISCUSSION

5.1. *Comparison with reported clusters*

Based on *Gaia* data, several OC-hunting studies have published more than 3000 OCs by applying multifarious clustering algorithms or manually searching approaches. We collected the published OCs within 500 pc from previous works (Liu & Pang 2019; Sim et al. 2019; Cantat-Gaudin et al. 2020; Hunt & Reffert 2021; He et al. 2022b,a; Li et al. 2022, hereafter LP19, Sim19, CG20, HR21, He22a, He22b, Li22 respectively), including about 10% of the OCs within 500 pc of the solar neighborhood. Many nearby young associations and moving groups within 500 pc to the Sun also have been investigated with *Gaia* data, such as the Orion complex with the strong sign of radial expansion attributed to a supernova expansion (Kounkel et al. 2018, hereafter K18), Vela OB2 hosts complex spatial filamentary substructures (Cantat-Gaudin et al. 2019; Beccari et al. 2020; Pang et al. 2021, hereafter CG19, B20, Pang21), Taurus region consists of 22 groups (Liu et al. 2021, hereafter Liu21), Chamaeleon I with two sub-clusters (Roccatagliata et al. 2018, hereafter R18), Corona Australis with “off-cloud” and “on-cloud” populations (Galli et al. 2020a, hereafter G20a), ϵ Cha Association (Dickson-Vandervelde et al. 2021, hereafter DV21), ρ Ophiuchi with two young populations (Grasser et al. 2021, hereafter G21), Perseus with five clustered group Autochthe, Alcaeus, Mestor, Electryon and Heleus (Pavlidou et al. 2021, hereafter P21), stellar ‘snake’ (Tian 2020; Wang et al. 2022, hereafter T20, W22), Lupus association (Galli et al. 2020b, hereafter G20b) and etc. We combined these published OCs as well as young associations and moving groups related to giant molecular clouds to create a reference cluster catalog (hereafter ref_OCs).

In order to carefully analyze the differences between the OCSN catalog and the ref_OCs catalog, we created a common sample for comparison. However, it is not appropriate to simply cross-match with two cluster catalogs through their center celestial coordinates. This is because the search area in our work (OCSN catalog) is systematically larger than many previous works (ref_OCs catalog), and the deviation of the cluster center coordinates derived by different methods in different works may be very large. Hence, we adopted cross-matching with all cluster members rather than the cluster itself.

Finally, with a matching radius of $1''$, a common catalog of about 332,000 members was obtained, which is referred to as the common_memb catalog.

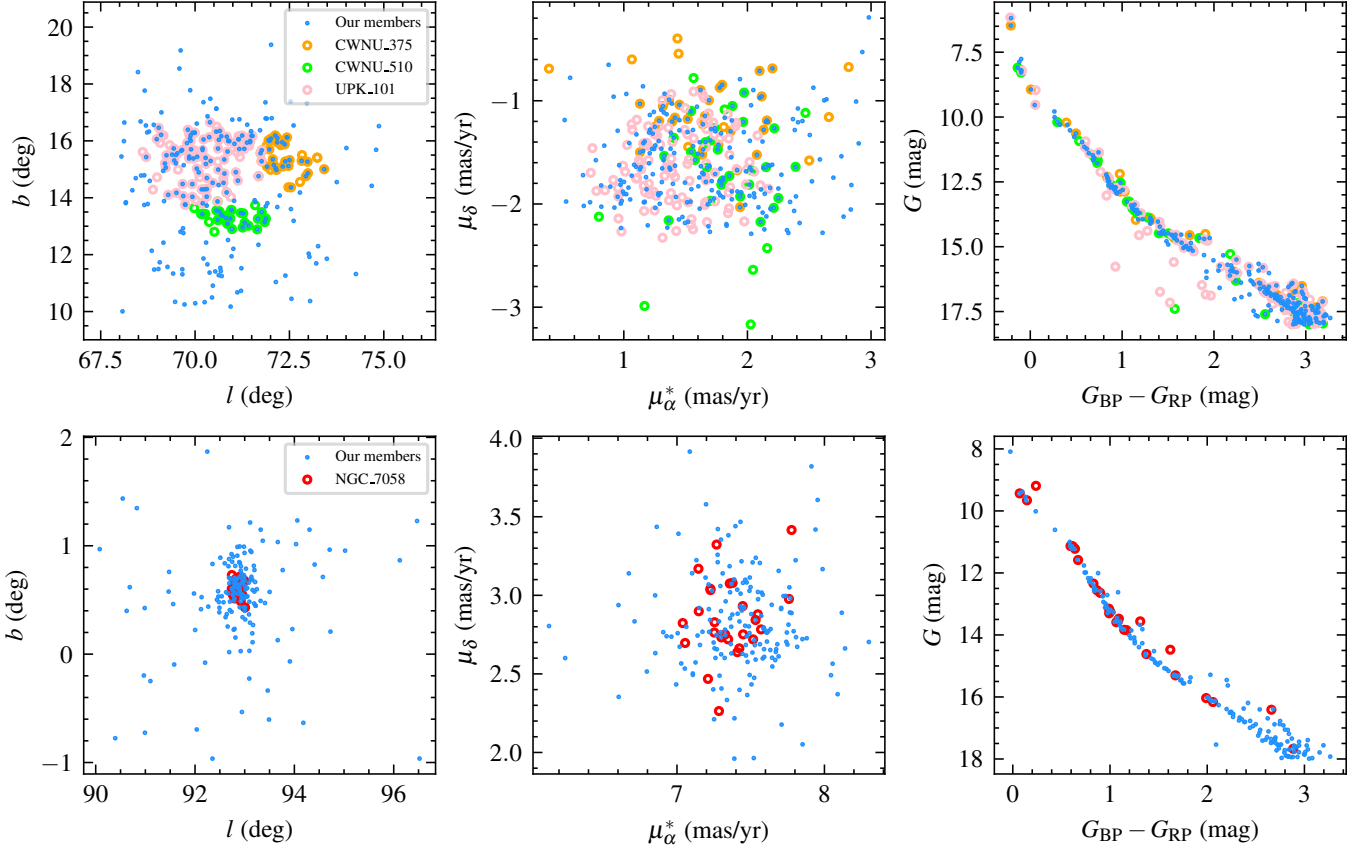


Figure 7. Example of the results of our searching procedure for two clusters. For each cluster, the three scatter plots (from left to right) represent the galactic coordinate distribution, proper motion distribution and CMD. The blue dots refer to the members identified in this work. The orange, green, pink, and red circles represent the members of CWNU_375 and CWNU_510 from He22a, UPK_101 from Sim19, NGC_7058 from CG20 respectively. CWNU_375 and UPK_101 have 4 common members, and CWNU_510 and UPK_101 have 3 common members in previous results.

For each cluster, we calculated the fraction (f) between the common member stars to members in the OCSN catalog and then assigned a flag according to this fraction. Meanwhile, we checked the position, proper motion, and parallax distribution of those common members through visual inspection to assess whether they are the same clusters. In our catalog, we provided the corresponding OC_flag of the cluster as well as its literature name in Table 2, which mainly have three cases below:

- (1) $OC_flag = 1$: $f = 0\%$, the new OCs in the OCSN catalog.
- (2) $OC_flag = 2$: $f < 50\%$ and most of the common members are located on the outer part of the cluster in the OCSN catalog.
- (3) $OC_flag = 3$: $f > 50\%$ or most of the common members are located in the center part of the cluster in the OCSN catalog.

For clusters whose $f < 50\%$, we further inspected the 5-dimension distribution of their members. For instance, the top panels in Figure 7 show the spatial, proper motion, and color-magnitude distributions of members of the three reported clusters. The reported cluster called CWNU_375, CWNU_510 are both published in He22a, and the UPK_101 are published in Sim19. The space distribution clearly shows that the cluster identified in the OCSN catalog incorporates the three reported clusters. In this case, the three reported clusters are regarded as reference clusters that combined as one cluster with $OC_flag = 2$ in the OCSN catalog (see Table 2). Similarly, the bottom panels in Figure 7 show another cluster case with $OC_flag = 3$. For this cluster, our work identified more members in a wider range, while the previously reported members of the cluster (NGC_7058) in CG20 are only a core component of this cluster. Finally, 25 OCs with $OC_Flag = 2$ and 198 OCs with $OC_Flag = 3$ were reported in the previous catalogs, and 101 new OCs with $OC_Flag = 1$ were not presented in any literature studies. We noticed that about 10% of our cataloged clusters coincided with known associations and moving groups, which clearly indicates that not all of the clusters are bound open clusters.

Figure 8 shows the distribution of 324 OCSN clusters in the Galactic coordinates, while the blue circle represents the half-number radius (r_h) of each cluster. Furthermore, we use the red squares and black dots to present the new OCs ($OC_flag = 1$) and reported OCs ($OC_flag = 2,3$) respectively. It is worth noting that many nearby clusters with large spatial scale (r_h) were discovered for the first time in our work. This also shows that our slicing approach is very effective for searching nearby OCs with a large spatial distribution.

For OCSN clusters that have been reported, we also compared their number of members, the half-number radius in physical sizes, and the age with the literature results. Figure 9 shows the comparison results, while the orange circles and blue dots present clusters whose `OC_flag=2` and `OC_flag=3` respectively. It can be seen that our cluster sample (especially the cluster with `OC_flag=2`) contains more member stars than the literature results. Moreover, because the r_h of most clusters is larger than previous results, the updated members in the cluster present a more extended spatial distribution. Our OCSN catalog expands the physical size of many nearby star clusters. On the other hand, because we only increased the number of member stars, the age of isochrone-fitting results of star clusters is still keeping consistent with the literature results.

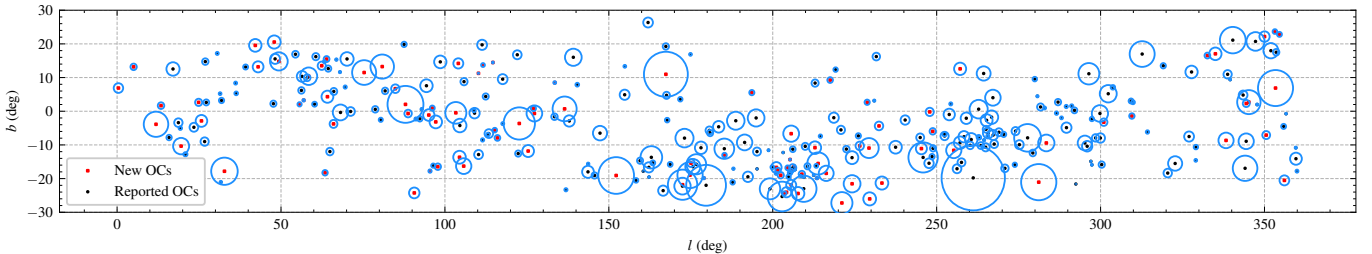


Figure 8. Distribution of the OC population in Galactic coordinates. The black points represent the reported OCs found in this study, and the red squares represent the OCs newly identified in this work using Gaia DR3. The blue circles refer to the r_h given by this work.

5.2. Binary clusters

OCs are born in giant molecular clouds and in some cases also formed in groups (Camargo et al. 2016). A number of OCs are found in pairs or higher-order systems (Rozhavskii et al. 1976; Subramaniam et al. 1995; Soubiran et al. 2019). As the most famous double star clusters, h and χ Persei have been extensively studied and many interesting results have been obtained (Slesnick et al. 2002; Zhong et al. 2019; Li et al. 2019). Based on the high precision kinematic information provided by *Gaia* data, more and more binary clusters have been confirmed (Soubiran et al. 2019; Casado 2021; Bisht et al. 2021; Angelo et al. 2022), which is important for studying the formation and dynamical evolution of OCs (de La Fuente Marcos & de La Fuente Marcos 2009; de la Fuente Marcos & de la Fuente Marcos 2010; Arnold et al. 2017). We performed a preliminary screening in our cluster

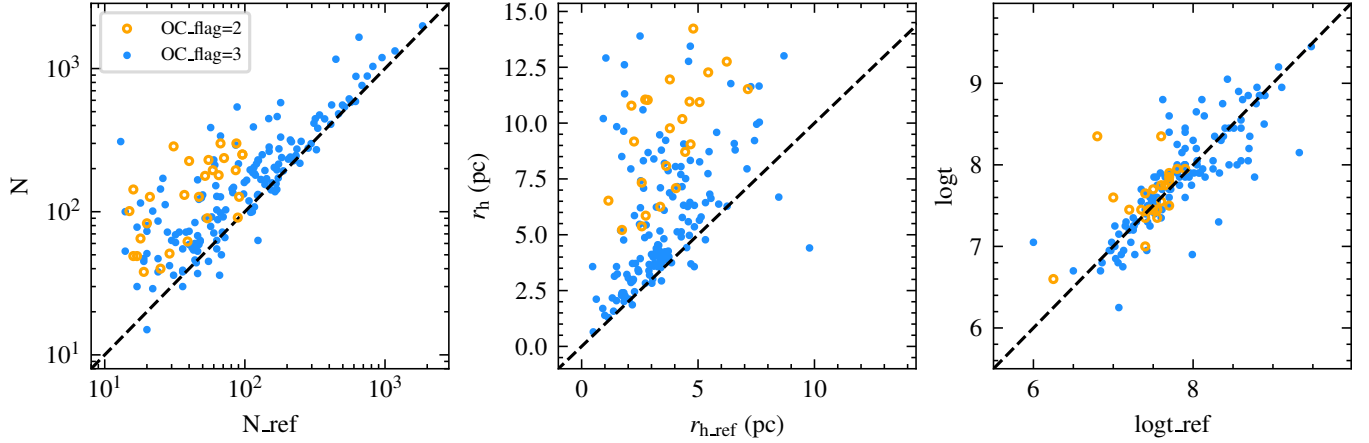


Figure 9. The comparison distribution of member numbers, r_h and age parameters between the reported clusters from ref_OC and the OCs obtained by this work. The blue dots refer to the OCs with “OC_flag” = 3 and the orange circles refer to the OCs with “OC_flag” = 2. The black dashed lines both show the relation of $y=x$.

samples with spatial separations $\Delta\text{pos} < 20$ pc (Subramaniam et al. 1995) and velocity differences $\Delta V < 5$ km s⁻¹ (Soubiran et al. 2019). As a result, we got 15 groups of OCs including binary and triple cluster systems. The results are listed in Table 5.

In our catalog, there are 19 open cluster pairs with a common origin, whose age differences are less than 30 Myr. We show a pair of two new OCs in Figure 10 : OCSN_98 and OCSN_100. It is clear that the mean central position of the two clusters is very close ($\Delta\text{pos} = 13$ pc), while the tangential velocities (black arrows in the left panel) and radial velocities (histogram in the middle panel) are also similar. The total velocity difference between the two clusters is $\Delta V = 1.3$ km s⁻¹. The absolute CMDs of the two clusters are presented in the right panel, which presents the same visual fitting age with $\text{log}t = 6.85$. The similarity of the two clusters suggests that they may have a common origin.

Furthermore, along with more new star clusters added, we found three groups (Group 3, Group 5, and Group 11 in Table 5) containing triple OCs, whose age differences are less than 10 Myr. For example, Group 3 comprises two new OCs and one already reported open cluster: OCSN_40, OCSN_41, and OCSN_158. As shown in Table 5, the two pairs of OCSN_40, OCSN_41 and OCSN_40, OCSN_158 have similar positions ($\Delta\text{pos} \approx 17$ pc) and similar velocities ($\Delta V < 3.5$ km s⁻¹). At the

same time, since these three clusters have almost the same age ($\text{logt} = 7.25, 7.20, 7.20$), it can be inferred that the triple clusters also formed together from the same molecular cloud.

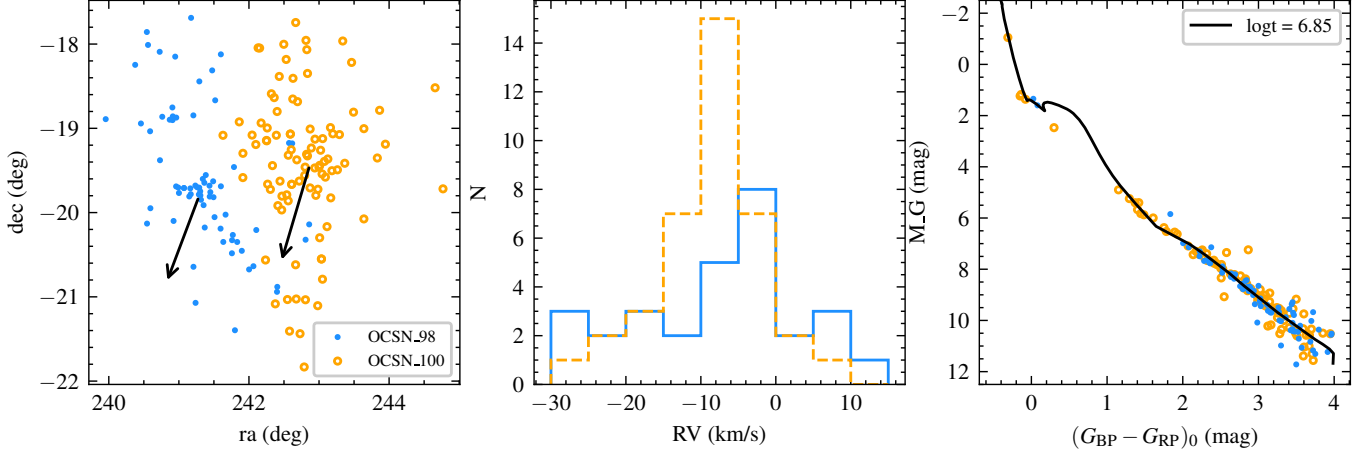


Figure 10. An example of binary cluster in our samples, OCSN_98 in blue and OCSN_100 in orange. Left panel: the spatial distribution for two OCs and the black arrows refer to their projected moving direction. Middle panel: the histograms of radial velocities for their members. Right panel: the absolute CMDs for two OCs and the black line refers to the isochrone with solar metallicity $Z_{\odot} = 0.0152$ (Caffau et al. 2009, 2011) and logarithm of age $\text{logt} = 6.85$.

6. SUMMARY

In this paper, we performed a systematically blind search for OCs at Galactic latitudes $|b| \leq 30^{\circ}$ within 500 pc of the solar neighborhood by choosing different slicing box sizes in different distance grids with *Gaia* DR3 data. By utilizing the clustering algorithms pyUPMASK and HDSBSCAN, we identified a total of 324 OCs. Our results include 101 new clusters that were never reported before, increasing the OC census within 500 pc by about 50%. Meanwhile, 223 reported clusters and their members were updated by carefully comparing the spatial distribution and other properties with the previous cluster catalog (ref_OC). In the OCSN catalog, we provided the membership probabilities of member stars and further estimated the mean positions, proper motions, parallaxes, and structural parameters for each cluster. We also derived mean radial velocities of OCs through the Gaussian fitting based on *Gaia* DR3. Subsequently, we performed the visual isochrone-fitting to obtain the

Table 5. Binary clusters in our OC sample.

Group	cluster1	cluster2	Δ_{pos} (pc)	ΔV (km s ⁻¹)
1	OCSN_16	OCSN_18	15.9	1.4
2	OCSN_29	OCSN_286	16.8	2.8
3	OCSN_40	OCSN_41	17.1	1.0
3	OCSN_40	OCSN_158	17.5	3.5
4	OCSN_50	OCSN_51	12.3	3.4
5	OCSN_91	OCSN_92	6.5	3.6
5	OCSN_91	OCSN_237	19.9	1.6
5	OCSN_92	OCSN_237	17.1	2.3
6	OCSN_98	OCSN_100	13.1	1.3
7	OCSN_118	OCSN_271	16.5	1.0
8	OCSN_124	OCSN_184	16.8	3.8
9	OCSN_127	OCSN_129	13.2	1.7
10	OCSN_128	OCSN_283	18.1	2.4
11	OCSN_176	OCSN_178	18.9	0.8
11	OCSN_177	OCSN_178	12.7	2.1
12	OCSN_187	OCSN_188	5.6	4.3
13	OCSN_197	OCSN_198	18.2	1.4
14	OCSN_245	OCSN_246	10.0	3.5
15	OCSN_322	OCSN_324	10.9	2.4

ages, distance modulus, and reddening values for the clusters according to the distribution of member stars on the CMDs.

In particular, we compared the star clusters in the literature with our star clusters and use an OC_flag to classify the OCSN clusters into three samples. Our classification based on manual inspection not only marks new clusters but also combines some duplicate or partially reported clusters. Additionally, 19 pairs of clusters were identified as binary clusters in the solar neighborhood, and 3 groups of OCs were confirmed as triple cluster systems, with spatial separation less than 20 pc, velocity difference less than 5 km s^{-1} , and similar ages.

For our hunted OC samples within 500 pc in the solar neighborhood, more detailed analyses are needed to further investigate their properties, such as the mass function and the dynamical states. Especially more spectroscopic data for the member stars will be of prime importance to determine the dynamical and chemical evolution of these clusters.

This work is supported by the National Key R&D Program of China No. 2019YFA0405501. Li Chen acknowledges the support from the National Natural Science Foundation of China (NSFC) through grants 12090040 and 12090042. Jing Zhong would like to acknowledge the NSFC under grant 12073060, and the Youth Innovation Promotion Association CAS. We acknowledge the science research grants from the China Manned Space Project with NO. CMS-CSST-2021-A08.

This work has made use of data from the European Space Agency (ESA) mission *Gaia* (<https://www.cosmos.esa.int/gaia>), processed by the *Gaia* Data Processing and Analysis Consortium (DPAC, <https://www.cosmos.esa.int/web/gaia/dpac/consortium>). Funding for the DPAC has been provided by national institutions, in particular, the institutions participating in the *Gaia* Multilateral Agreement.

REFERENCES

- | | |
|--|---|
| <p>Abdurro'uf, Accetta, K., Aerts, C., et al. 2022, <i>ApJS</i>, 259, 35</p> <p>Angelo, M. S., Santos, J. F. C., Maia, F. F. S., & Corradi, W. J. B. 2022, <i>MNRAS</i>, 510, 5695</p> | <p>Arnold, B., Goodwin, S. P., Griffiths, D. W., & Parker, R. J. 2017, <i>MNRAS</i>, 471, 2498</p> <p>Bai, L., Zhong, J., Chen, L., Li, J., & Hou, J. 2022, <i>Research in Astronomy and Astrophysics</i>, 22, 055022</p> |
|--|---|

- Beccari, G., Boffin, H. M. J., & Jerabkova, T. 2020, *MNRAS*, 491, 2205
- Bisht, D., Zhu, Q., Yadav, R. K. S., et al. 2021, *MNRAS*, 503, 5929
- Boffin, H. M. J., Jerabkova, T., Beccari, G., & Wang, L. 2022, *MNRAS*, 514, 3579
- Caffau, E., Ludwig, H. G., Steffen, M., Freytag, B., & Bonifacio, P. 2011, *SoPh*, 268, 255
- Caffau, E., Maiorca, E., Bonifacio, P., et al. 2009, *A&A*, 498, 877
- Camargo, D., Bica, E., & Bonatto, C. 2016, *MNRAS*, 455, 3126
- Campello, R. J. G. B., Moulavi, D., & Sander, J. 2013, in *Pacific-Asia Conference on Knowledge Discovery and Data Mining*
- Cantat-Gaudin, T., Jordi, C., Vallenari, A., et al. 2018, *A&A*, 618, A93
- Cantat-Gaudin, T., Jordi, C., Wright, N. J., et al. 2019, *A&A*, 626, A17
- Cantat-Gaudin, T., Anders, F., Castro-Ginard, A., et al. 2020, *A&A*, 640, A1
- Carrera, R., Pasquato, M., Vallenari, A., et al. 2019, *A&A*, 627, A119
- Casado, J. 2021, *Astronomy Reports*, 65, 755
- Casagrande, L., & VandenBerg, D. A. 2018, *MNRAS*, 479, L102
- Castro-Ginard, A., Jordi, C., Luri, X., et al. 2020, *A&A*, 635, A45
- . 2022, *A&A*, 661, A118
- Chaturvedi, A., Green, P. E., & Carroll, J. D. 2001, *Journal of Classification*, 18, 35
- de La Fuente Marcos, R., & de La Fuente Marcos, C. 2009, *A&A*, 500, L13
- de la Fuente Marcos, R., & de la Fuente Marcos, C. 2010, *ApJ*, 719, 104
- Dias, W. S., Alessi, B. S., Moitinho, A., & Lépine, J. R. D. 2002, *A&A*, 389, 871
- Dias, W. S., & Lépine, J. R. D. 2005, *ApJ*, 629, 825
- Dickson-Vandervelde, D. A., Wilson, E. C., & Kastner, J. H. 2021, *AJ*, 161, 87
- Donor, J., Frinchaboy, P. M., Cunha, K., et al. 2020, *AJ*, 159, 199
- Ester, M., Kriegel, H. P., Sander, J., & Xu, X. 1996, *AAAI Press*
- Evans, Neal J., I., Dunham, M. M., Jørgensen, J. K., et al. 2009, *ApJS*, 181, 321
- Fouesneau, M., Frémat, Y., Andrae, R., et al. 2022, *arXiv e-prints*, arXiv:2206.05992
- Gaia Collaboration, Brown, A. G. A., Vallenari, A., et al. 2018, *A&A*, 616, A1
- . 2021, *A&A*, 649, A1
- Gaia Collaboration, Vallenari, A., Brown, A. G. A., et al. 2022, *arXiv e-prints*, arXiv:2208.00211
- Galli, P. A. B., Bouy, H., Olivares, J., et al. 2020a, *A&A*, 634, A98
- . 2020b, *A&A*, 643, A148
- Ginsburg, A., Sipőcz, B. M., Brasseur, C. E., et al. 2019, *AJ*, 157, 98
- Grasser, N., Ratzenböck, S., Alves, J., et al. 2021, *A&A*, 652, A2

- He, Z., Wang, K., Luo, Y., et al. 2022a, *ApJS*, 262, 7
- He, Z., Li, C., Zhong, J., et al. 2022b, *ApJS*, 260, 8
- Heyl, J., Caiazzo, I., & Richer, H. B. 2022, *ApJ*, 926, 132
- Huchra, J. P., & Geller, M. J. 1982, *ApJ*, 257, 423
- Hunt, E. L., & Reffert, S. 2021, *A&A*, 646, A104
- Janes, K., & Adler, D. 1982, *ApJS*, 49, 425
- Katz, D., Sartoretti, P., Guerrier, A., et al. 2022, arXiv e-prints, arXiv:2206.05902
- Kharchenko, N. V., Piskunov, A. E., Schilbach, E., Röser, S., & Scholz, R. D. 2013, *A&A*, 558, A53
- King, I. 1962, *AJ*, 67, 471
- King, I. R. 1966, *AJ*, 71, 276
- Kounkel, M., Covey, K., Suárez, G., et al. 2018, *AJ*, 156, 84
- Krone-Martins, A., & Moitinho, A. 2014, *A&A*, 561, A57
- Lada, C. J., & Lada, E. A. 2003, *ARA&A*, 41, 57
- Li, C., Sun, W., de Grijs, R., et al. 2019, *ApJ*, 876, 65
- Li, Z., Deng, Y., Chi, H., et al. 2022, *ApJS*, 259, 19
- Lindgren, L. 2018, gAIA-C3-TN-LU-LL-124. http://www.rssd.esa.int/doc_fetch.php?id=3757412
- Liu, J., Fang, M., Tian, H., et al. 2021, *ApJS*, 254, 20
- Liu, L., & Pang, X. 2019, *ApJS*, 245, 32
- Marigo, P., Girardi, L., Bressan, A., et al. 2017, *ApJ*, 835, 77
- McInnes, L., Healy, J., & Astels, S. 2017a, *The Journal of Open Source Software*, 2, 205. <http://joss.theoj.org/papers/10.21105/joss.00205>
- . 2017b, *The Journal of Open Source Software*, 2, 205
- Meingast, S., & Alves, J. 2019, *A&A*, 621, L3
- Meingast, S., Alves, J., & Rottensteiner, A. 2021, *A&A*, 645, A84
- Netopil, M., Oralhan, İ. A., Çakmak, H., Michel, R., & Karataş, Y. 2022, *MNRAS*, 509, 421
- Netopil, M., Paunzen, E., & Carraro, G. 2015, *A&A*, 582, A19
- Pang, X., Yu, Z., Tang, S.-Y., et al. 2021, *ApJ*, 923, 20
- Pavlidou, T., Scholz, A., & Teixeira, P. S. 2021, *MNRAS*, 503, 3232
- Pearson, K. 1894, *Philosophical Transactions of the Royal Society of London Series A*, 185, 71
- Pera, M. S., Perren, G. I., Moitinho, A., Navone, H. D., & Vazquez, R. A. 2021, *A&A*, 650, A109
- Portegies Zwart, S. F., McMillan, S. L. W., & Gieles, M. 2010, *ARA&A*, 48, 431
- Riello, M., de Angeli, F., Evans, D. W., et al. 2021, *VizieR Online Data Catalog*, J/A+A/649/A3
- Ripley, B. D. 1976, *Journal of Applied Probability*, 13, 255
- Roccatagliata, V., Sacco, G. G., Franciosini, E., & Randich, S. 2018, *A&A*, 617, L4
- Rodriguez, A., & Laio, A. 2014, *Science*, 344, 1492
- Rozhavskii, F. G., Kuz'mina, V. A., & Vasilevskii, A. E. 1976, *Astrophysics*, 12, 204

- Scott, D. W. 1992, in *Multivariate Density Estimation: Theory, Practice, and Visualization*
- Scott, D. W. 2015, in *Multivariate Density Estimation: Theory, Practice, and Visualization, Second Edition*
- Sculley, D. 2010, in *International Conference on World Wide Web*
- Sim, G., Lee, S. H., Ann, H. B., & Kim, S. 2019, *Journal of The Korean Astronomical Society*, 52, 145.
<https://doi.org/10.5303/JKAS.2019.52.5.145>
- Slesnick, C. L., Hillenbrand, L. A., & Massey, P. 2002, *ApJ*, 576, 880
- Soubiran, C., Cantat-Gaudin, T., Romero-Gómez, M., et al. 2019, *A&A*, 623, C2
- Subramaniam, A., Gorti, U., Sagar, R., & Bhatt, H. C. 1995, *A&A*, 302, 86
- Tarricq, Y., Soubiran, C., Casamiquela, L., et al. 2022, *A&A*, 659, A59
- Tian, H.-J. 2020, *ApJ*, 904, 196
- Voronoi, M. G. 1908, 97
- Wang, F., Tian, H., Qiu, D., et al. 2022, *MNRAS*, 513, 503
- Ye, X., Zhao, J., Oswald, T. D., Yang, Y., & Zhao, G. 2022, arXiv e-prints, arXiv:2207.14229
- Zepeda-Mendoza, M. L., & Resendis-Antonio, O. 2013, *Encyclopedia of Systems Biology*, 43, 886
- Zhang, Y., Tang, S.-Y., Chen, W. P., Pang, X., & Liu, J. Z. 2020, *ApJ*, 889, 99
- Zhong, J., Chen, L., Jiang, Y., Qin, S., & Hou, J. 2022, *AJ*, 164, 54
- Zhong, J., Chen, L., Kouwenhoven, M. B. N., et al. 2019, *A&A*, 624, A34
- Zhong, J., Chen, L., Wu, D., et al. 2020, *A&A*, 640, A127